Check for updates

ADVANCED FUNCTIONAL MATERIALS
www.afm-journal.de

Bidirectional Lambertian Scatterers Using Acoustic Holograms for the Simultaneous Control of Reflected and Transmitted Wavefronts

Eric Ballestero, Josep Rodriguez-Sendra, Vicent Romero-García, Jean-Philippe Groby, and Noé Jiménez*

Acoustic holography enables the creation of tailored spatiotemporal wavefield distributions. In this study, the design of acoustic holograms that simultaneously control both the reflected and the transmitted fields are presented. This is accomplished through the use of a bidirectional metasurface, which encodes the phase of a desired wavefront in a discrete spatial distribution of monolithic sub-elements. This approach is employed in particular to design an optimized hologram that behaves as an ideal Lambertian scatter for both reflection and transmission. The design follows a quadratic-residue sequence, with theoretical results validated both numerically and experimentally. It is observed that this kind of structure produces a uniform scattering response, with a high diffusion coefficient of approximately 0.7 and a correlation scattering coefficient of 0.98 in both transmission and reflection. The hologram demonstrates the potential to significantly reduce imaging artefacts in ultrafast ultrasound techniques in strongly reverberating environments, as evidenced by examples.

1. Introduction

Over the past decade, the use of acoustic holograms[1,2] has been a key research topic for wavefront shaping in acoustics and ultrasonics. Acoustic holograms are able to generate arbitrary acoustic fields, typically producing complex images, by encoding specific phase and magnitude patterns. Usually, acoustic holograms are encoded in a passive structure, e.g., in a 3D-printed structure, and when an acoustic wave is reflected or transmitted through it, the target field is generated. At the beginning, phase-only holograms where proposed to synthesize fields in transmission[1–5] and, later, in reflection.[6,7] Several strategies for amplitude and phase modulation have been proposed for acoustics in air[8,9] and ultrasonics in water.[3,10,11] Multiple images can be produced by the same hologram using different frequencies.[12]

Holograms have been used for many practical applications,[13] like particle trapping, manipulation and patterning,[14–17] 3D-printing,[18,19] exotic and vortex beam generation,[20–22] haptic devices[23] or volumetric displays.[24] Mainly triggered by the wide accessibility to modern 3D-printed technologies, holograms have also found practical application in biomedical ultrasound as a low-cost strategy for wavefront engineering. Traditionally, acoustic beamforming relied on phased-array systems, where the phases and amplitudes are controlled using multichannel transducers and electronics. While these devices are used in common medical practice, the poor channel scalability of their radio-frequency electronics, currently up to 1024 channels, limits their wavefront shaping performance.[25] In contrast, the pixel density in acoustic holograms can be three or four orders of magnitude higher,[26] enabling complex image formation into biological tissues. Holograms have been tested for aberration compensation in transcranial ultrasound therapy, where the acoustic image can match therapeutic targets in the central nervous system,[26] controlling the spatial distribution of thermal patterns for hyperthermia treatments,[27–29] controlling cavitation patterns,[30] produce localized drug delivery in the brain in arbitrary areas,[31] neuromodulation[32] or transcranial vortex generation.[33] For imaging, holograms have been proposed for single-element imaging using compressive sensing,[34] for local cavitation monitoring using holograms and passive cavitation beamforming,[35] or high-resolution 4D imaging.[36]

Holograms can also be used to tailor scattering patterns. For example, an acoustic vortex can be encoded in a holographic metasurface to produce a scattering with no specular reflection.[37] Indeed, encoding a reflected wave-field in a passive structure has been applied for decades in concert hall acoustics using acoustic diffusers.[38,39] Using phase grating acoustic

E. Ballestero, J.-P. Groby
Laboratoire d'Acoustique de l'Université du Mans (LAUM), UMR 6613
Institutd'Acoustique - Graduate School (IA-GS), CNRS, Le Mans Université
Le Mans 72085, France
E-mail: eric.ballestero@univ-lemans.fr
J. Rodriguez-Sendra, N. Jiménez
Instituto de Instrumentación para Imagen Molecular
Consejo Superior de Investigaciones Científicas (CSIC)
Universitat Politècnica de València
València 46022, Spain
V. Romero-García
Instituto Universitario de Matemática Pura y Aplicada (IUMPA)
Universitat Politècnica de València
València 46022, Spain

DOI: 10.1002/adfm.202423715

 © 2025 Wiley-VCH GmbH

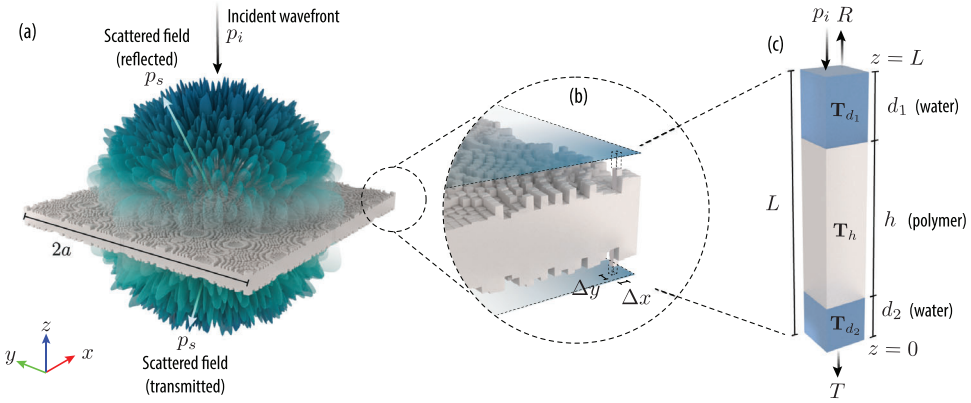


Figure 1. a) Scheme of the bidirectional ultrasonic hologram and the uniform scattering pattern, an incident plane wave in arbitrary uniform scattering profiles for each direction; b) Close-up of the lens; each monolithic block has a lateral size of $\Delta x \times \Delta y = 700\ \mu m \times 700\ \mu m$, and the total width of the structure is $2a$. c) Representation of the 1D Transfer Matrix Method diagram of a monolithic block of total length L composed of a solid slab (polymer) and the surrounding fluid layers (water).

diffusers, the phase of the reflected sound varies according to the depth of a series of tailored wells acting as quarter-wavelength resonators. Other approaches include the use of Helmholtz resonators and slow sound metamaterials to reduce the thickness of these structures.[40] Concert hall acoustic diffusers have been proven to reduce the specular reflection of objects,[41] or to help distribute wave-fields evenly in space and time.[42] However, these structures only work in reflection due to the reflecting nature of manufacturing materials for audible sound. Recently, structures have been proposed to control the scattering of reflected and transmitted sound waves in the audible regime.[43–45] Such structures could also be used directly in reflection situations for reducing unwanted specular reflections, e.g., reflections from surgical instruments during ultrasound-guided medical procedures.[46]

In this work, we present a bidirectional asymmetric ultrasonic hologram that can simultaneously control both the reflected and transmitted wave-fields. To do that, we design a metasurface made of a discrete spatial distribution of elastic slabs, as shown in **Figure 1**. This approach allows encoding a given wavefield in transmission and reflection into a single monolithic 3D-printed structure. In particular, we designed a bidirectional hologram to produce a diffuse scattering pattern, evenly distributing energy along the whole angular spectrum, acting as a Lambertian metasurface in analogy with perfect optical diffusers in optics.[47] This acoustic structure can be useful to reduce unwanted specular reflections for biomedical ultrasound applications, as shown in the example in the last section of this paper using ultrafast ultrasound imaging.

2. Results

2.1. Bidirectional Monolith Optimization

We consider an ultrasonic hologram composed of a discrete spatial distribution of building blocks made of monolithic elastic blocks (polymer) of different height embedded in a fluid (water). An illustration of the hologram is shown in Figure 1 and the mathematical derivations for asymmetric wave propagation in and out of each single monolithic block, along with material properties, can be found in the Experimental Section. However, one important operation before designing this hologram is to find a set of monolithic polymer block lengths, h, as well as the length of the water blocks d_1 (starting from L down to L/2) and d_2 (from 0 up to L/2), given a total system height $L = d_1 + h + d_2$, in order to cover all the combinations for the phase of the reflection, φ_R, and transmission, φ_T, coefficients. While the functions $R(d_1, h, d_2)$ and $T(d_1, h, d_2)$ are continuous, we propose to obtain a finite set of combinations[9] by discretizing the phase-space in N_φ^2 possible values.

In this way, we look for the geometrical parameters $d_1(\varphi_R, \varphi_T)$, $h(\varphi_R, \varphi_T)$, and $d_2(\varphi_R, \varphi_T)$ that generate all the combinations of the phases $\varphi_R(i)$, and $\varphi_T(j)$, where $i = 0, ..., N_\varphi, j = 0, ..., N_\varphi$, $\varphi_R(i) = -\pi + 2i\pi/N_\varphi$ and $\varphi_T(j) = -\pi + 2j\pi/N_\varphi$. We choose $N_\varphi = 21$ as the total amount of discrete radian steps, providing in this case resolution steps representing approximately 5% of the total angular unit circle. This choice is here justified by the fact that (i) in this work we are not really interested in finding the minimal length of material that would be required to provide any phase combination but rather one that could fit depending on a set of custom application-driven manufacturing constraints, and (ii), the phase discretization resulting from a very small manufacturing resolution could significantly increase the phase-space matrix, and thus proportionally lengthen the following optimization process for finding phase-space combinations, as discussed below.

To find the geometrical parameters (h, d_1, d_2), a multi-objective minimization method based on genetic algorithms is used, with lower and upper boundaries on d_1 and d_2 such that $d_n \in [0, 0.95L]$ in order to maintain a common material section between blocks for manufacturing concerns. The multi-objective optimization algorithm would then yield a set of plausible solutions that can achieve the required couple of phase combinations $\varphi_R(i)$ and $\varphi_T(j)$. Indeed, more than one solution satisfying the optimization goals generally exists in this problem, i.e., the set of solutions composing the Pareto front. The multi-objective minimization algorithm would thus minimize the following cost functions for the i-th and j-th combination

$$\epsilon_1(h, d_1, d_2) = \left|\varphi_R(i) - \arg[R_{\mathrm{TMM}}(l, d_1, d_2)]\right|/2\pi \quad (1)$$

© 2025 Wiley-VCH GmbH

16163028, 0, Downloaded from https://advanced.onlinelibrary.wiley.com/doi/10.1002/adfm.202423715 by Universitaet Politecnica De Val, Wiley Online Library on [06/03/2025]. See the Terms and Conditions (https://onlinelibrary.wiley.com/terms-and-conditions) on Wiley Online Library for rules of use; OA articles are governed by the applicable Creative Commons License

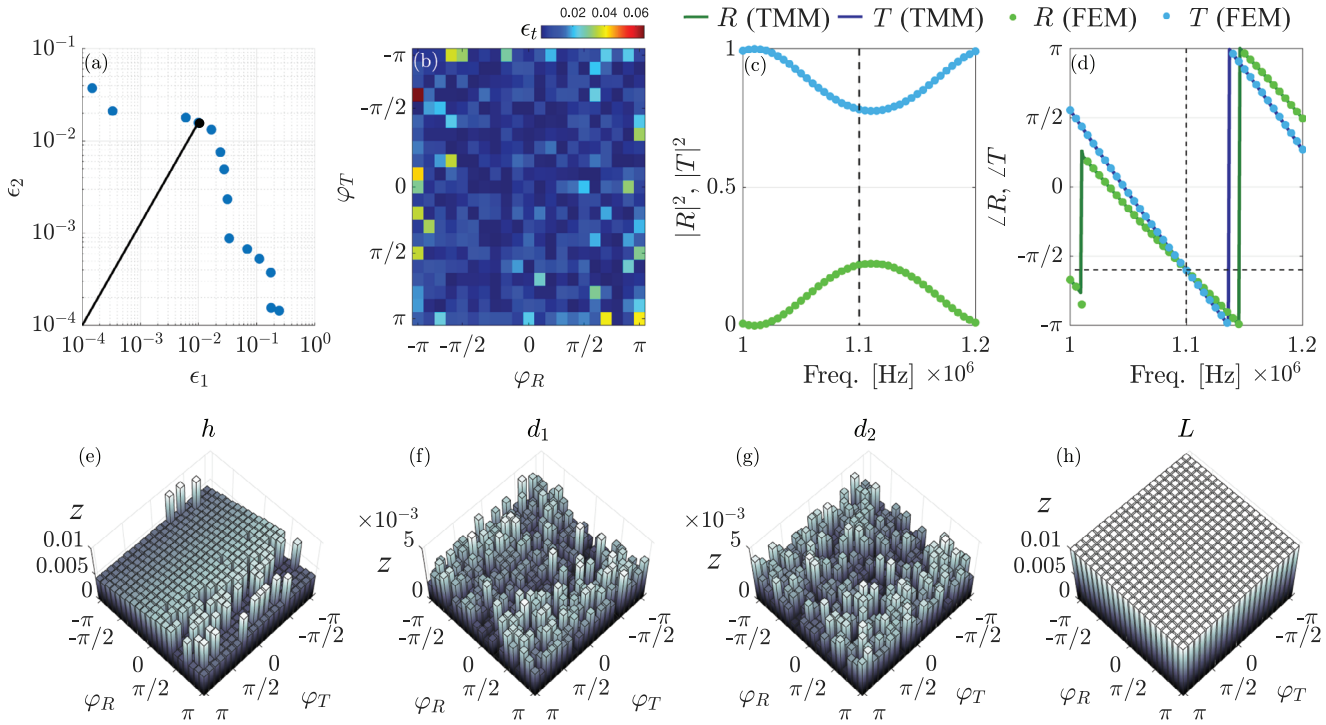


Figure 2. a) Multi-objective Pareto front for a single pixel of the hologram. The selected minima of the Pareto front is represented in black. b) Cost function error $\epsilon_t = \epsilon_1 + \epsilon_2$ at the end of the multi-objective minimization, as a function of the phase of the reflection and transmission coefficients. c) Magnitude and d) phase of the 1D reflection and transmission coefficients of an optimized polymer block length which satisfies $\varphi_R = \varphi_T = -1.886$ rad, obtained analytically (TMM) and numerically (FEM). e–h) Phase-space representation of the optimized lengths $h(\varphi_R, \varphi_T)$, $d_1(\varphi_R, \varphi_T)$, $d_2(\varphi_R, \varphi_T)$, and $L = h + d_1 + d_2$, respectively.

$$\epsilon_2(h, d_1, d_2) = \left|\varphi_T(j) - \arg[T_{\mathrm{TMM}}(l, d_1, d_2)]\right|/2\pi \tag{2}$$

where $\arg(\cdot) = \tan(\mathrm{Im}(\cdot)/\mathrm{Re}(\cdot))$ symbolizes the phase angle, $\varphi_R(i)$ and $\varphi_T(j)$ are the objective phases, and R_{TMM} and T_{TMM} are the reflection and transmission coefficients obtained using the TMM model given by Equations (10,11). The 2π denominator is used for normalizing the cost function in an interval [0,1]. Then, for each i-th and j-th element of the target phase-space, the multi-objective optimization problem can be formulated as

$$\min_{(h,d_1,d_2)\in\mathbb{R}} \left[\epsilon_1(h, d_1, d_2), \epsilon_2(h, d_1, d_2)\right] \tag{3}$$

Although the Pareto set represents a set of plausible geometrical parameters than can fit the minimization problem, only one solution per combination is needed to design the structure. Here, we will take the solution that presents a minimum distance from the ideal point $(\epsilon_1, \epsilon_2) = 0$, as shown in **Figure 2a**. This selection can only be performed since the solutions and their relative cost functions are of the same type. Figure 2b depicts the sum of the cost functions, $\epsilon_t = \epsilon_1 + \epsilon_2$, for the retrieved combinations of φ_R and φ_T. As the cost functions have been normalized on a [0,1] interval, it can be seen that the sum of the cost functions is significantly low, with sparse maxima about two orders of magnitude below the maximum possible error (i.e., 1) and a vast amount of minima about three to six orders of magnitude lower. This demonstrates an excellent ability of the system to reproduce any kind of phase combinations.

A Finite Element Method (FEM) numerical validation using COMSOL Multiphysics was performed for a selected phase-space matrix element, corresponding to $\varphi_R = \varphi_T = -1.886$ rad. Figure 2c,d, display the magnitude and phase of reflection and transmission coefficients, respectively. An excellent agreement can be observed between the TMM theory and the FEM simulation. Figure 2c shows that the system presents maxima and minima of transmission coefficient (and conversely for the reflection coefficient). This implies that some hologram cells could potentially have a quasi-null reflection coefficient, letting all the ultrasonic waves pass. Due to the high variability of solutions that will be chosen, it is assumed that a relatively even distribution will be ultimately attained between full transmission and partial transmission blocks, ie., blocks with marginal reflection magnitudes. Concerning the phases of both reflection and transmission coefficients, it can be seen in Figure 2d that both phases converge toward the desired value (–1.886 rad) at the design frequency (1.1 MHz).

Figure 2e–h shows the retrieved geometrical parameters h, d_1, d_2 and $L = h + d_1 + d_2$ obtained for each phase combination, respectively. A remarkable feature of Figure 2e can be seen, where the length of polymer blocks increases almost linearly in function of the gradient of the transmission coefficient phase, and drops to minimal values (similar to the ones at $\varphi_T = -\pi$) around a transmission phase of $\pi/2$, which is linked to a phase shit of the transmission coefficient around such lengths h. Figure 2f,g representing the lengths d_1 and d_2 show an inversely correlated pattern with h, i.e., large h values lead to small d_1 and d_2 values.

© 2025 Wiley-VCH GmbH

16163028, 0, Downloaded from https://advanced.onlinelibrary.wiley.com/doi/10.1002/adfm.202423715 by Universitaet Politecnica De Val, Wiley Online Library on [06/03/2025]. See the Terms and Conditions (https://onlinelibrary.wiley.com/terms-and-conditions) on Wiley Online Library for rules of use; OA articles are governed by the applicable Creative Commons License

16163028, 0, Downloaded from https://advanced.onlinelibrary.wiley.com/doi/10.1002/adfm.202423715 by Universitaet Politecnica De Val, Wiley Online Library on [06/03/2025]. See the Terms and Conditions (https://onlinelibrary.wiley.com/terms-and-conditions) on Wiley Online Library for rules of use; OA articles are governed by the applicable Creative Commons License

This is expected as the system was designed in a way that $L = h + d_1 + d_2$. This is shown in Figure 2h by a uniform total length L distribution over the phase-space.

2.2. Design of a Quadratic Residue Hologram

In order to design a hologram that can behave as an ideal bidirectional diffuser, we look for a spatial phase distribution for both reflection and transmission coefficients such that the spatial Fourier transform of said distribution present a flat magnitude, i.e., energy is evenly distributed along the whole angular spectrum. There are many number theoretic sequences that can help design such phase distribution, such as the maximum length or quadratic residue sequences.[38] In this work, we make use of a quadratic residue (QR) to generate evenly spaced diffraction lobes with even energy (see Experimental Section for more details). A 2D QR-sequence composed of $N \times N$ elements can be expressed as[48]

$$s(n, m) = (n^2 + m^2)\mathrm{mod}(N) \tag{4}$$

where $n = 0, ..., N$ and $m = 0, ..., N$ are integers and indices of the sequence for the n-th and m-th element in the $x = n\Delta x$ and $y = m\Delta y$ directions, respectively, and mod refers to the *modulo* operator. When these sequences are proportional to the phase of a complex field in the form

$$\xi(x, y) = \exp(\mathrm{i}s(x, y)\pi/N) \tag{5}$$

the complex function $\xi(x, y)$ presents a flat spatial Fourier transform.[39] Therefore, these sequences can be used to design bidirectional acoustic diffusers when

$$\varphi_T(x, y) = \varphi_R(x, y) = s(x, y)\pi/N \tag{6}$$

and N is a prime number.

The last step for designing the bidirectional hologram remains to go over each element (n, m) of the hologram, located at coordinates (x, y), and find the geometrical parameters (h, d_1, d_2) associated to the phase combination element $\varphi_R(x, y)$ and $\varphi_T(x, y)$ given by Equation (6). These geometrical parameters, $d_1(\varphi_R, \varphi_T)$, $h(\varphi_R, \varphi_T)$, and $d_2(\varphi_R, \varphi_T)$, are provided by the above-mentioned optimization procedure.

2.3. Numerical Validation

A numerical validation was performed using a pseudo-spectral time-domain (PSTD) simulations method with a k-space corrector.[49] This method provides a low numerical dispersion over coarse computational grids, and it is convenient for use in ultrasonics where the domains can cover hundreds of wavelengths. A bidirectional ultrasonic hologram using $N = 11$ and $M = 3$ repetitions was designed, considering water with properties $c_0 = 1500$ m/s and $\rho_0 = 1000$ kg/m^3 for the surrounding media and a photo-polymer (Clear, FormLabs, USA) with properties $c_p = 2599$ m/s and $\rho_p = 1186$ kg/m^3, measured experimentally.[50] This material choice gives a ratio of $Z_p/Z_w = 1.67$, validating the model assumptions. The lateral size of each pixel was set to $\Delta x = \Delta y = 700$ µm, and the frequency was set to 1.1 MHz.

Figure 3a shows the 2D phase distribution in reflection, $\varphi_R(x, y)$. As shown previously in Figure 2b, the minimal deviations of the multi-objective cost function mean that the designed phase profile for each side would almost not deviate from the target. The corresponding magnitude, as the result of the TMM model, is shown Figure 3b. Ideally, the sequence presents a flat angular spectrum, and even considering variations in magnitude, the scattered field in the far field presents a flat spectrum distribution with high N peak values due to the periodicity of the repetitions, as shown in Figure 3c. A similar behavior is observed in transmission mode, note $\varphi_T(x, y) = \varphi_R(x, y)$, but in this case the magnitude of the transmission coefficient is closer to the unity, see Figure 3d–f, as a result of the chosen photo-polymer, whose properties are similar to water.

An important remark is that the theoretical phase distribution is discrete, and phase values given by the ideal sequence, Equation (6), are constant along each unit block. Of course, due to the continuity of pressure and particle velocities all over the theoretical surface, the pattern of the phase distribution in the near field may not show such discrete profile, as those presented in Figure 3 (a,d). In fact, this implies field discontinuities, that can only be achieved using evanescent components. If we filter the evanescent components using the angular spectrum method,[50,51] we obtain the field shown in Figure 3g,h for reflection and Figure 3j,k for transmission. At first, in the near field the filtered fields seem to differ from the theoretical QR sequence. However, evanescent components do not contribute to the far field and, therefore, the corresponding scattered field is quite close to the ideal, as shown in Figure 3i,l.

Indeed, the simulated reflected and transmitted fields, shown in Figure 3m,n,p,q, cannot describe the abrupt and discontinuous phase profile of the QR sequence. These simulated profiles are measured at the exit of the hologram, and many of the evanescent components may have lost their amplitude. However, the propagating modes of the simulated field actually capture the angular spectrum of the sequence. The near-field magnitude also presents the squared pattern, which emerged as a result of the interference of the multiple scattered waves traveling in N^2 directions covering the whole angular spectrum. As its angular spectrum is captured, the scattered far field also resembles the theoretical one as shown in Figure 3o,r for the reflected and transmitted modes. In addition, it has to be noted that the evanescent coupling at the interfaces and within the hologram caused by the coupling between neighboring reflected or transmitted waves, which are not accounted for in this model, may introduce some changes with respect to target values. This could explain the variations observed between theoretical and numerical phase distributions.

2.4. Experimental Far-Field Scattering

For the experimental validation, a larger 3D-printed hologram, with $N = 53$ repeated $M = 3$ times (see Figure 1a) was designed for a frequency of 1.1 MHz. The hologram was built using stereolithography technique (SLA). A high N value was taken in order to produce a large structure for ultrasonic measurements, where no more than $M = 3$ repetitions were desired to reduce

 © 2025 Wiley-VCH GmbH

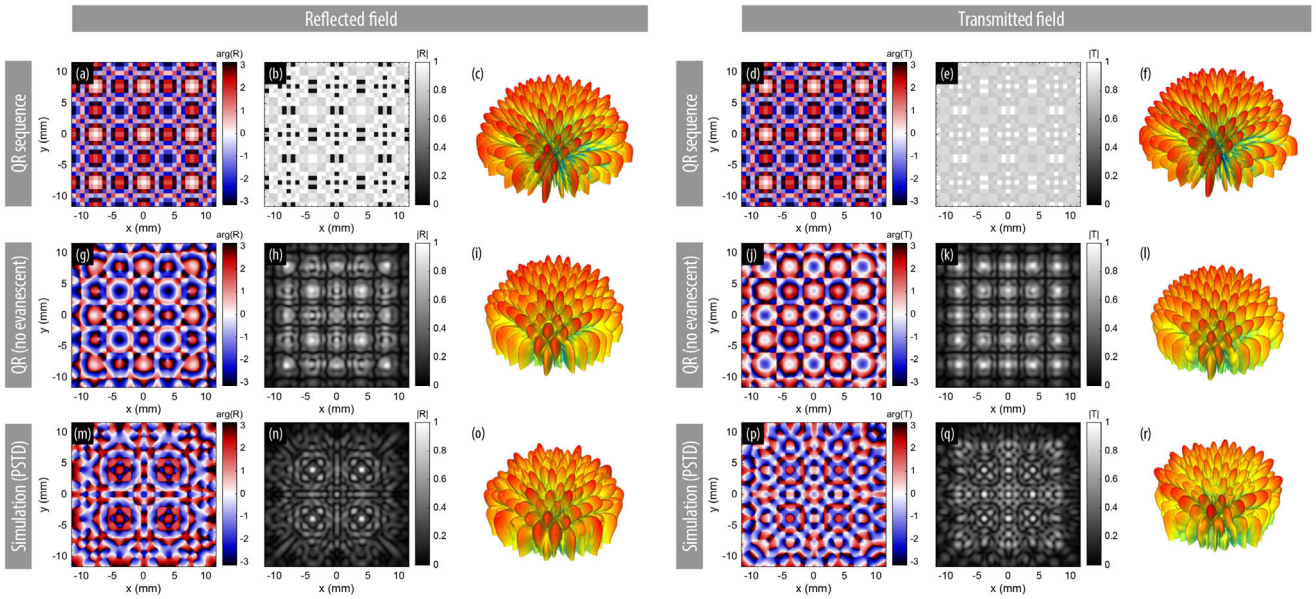


Figure 3. Theoretical 2D surface phase (a,d) and magnitude (b,e) distributions of the reflected and transmitted fields, respectively, of a 11 × 11 2D QR sequence repeated $M = 3$ times. c,f) Polar scattered fields of the QR sequence in reflection and transmission. g–l) Filtering evanescent components out of the QR sequence. m–r) Pseudo-spectral time-domain (PSTD) simulations.

diffraction grating lobes due to periodicity. A larger N also helps design a hologram with a much more uniform spatial Fourier transform due to the nature of pseudo-random sequences. Acoustic pressure was measured in front of the hologram in the x and y directions in order to map the near-field pressure plane distribution, at $z = 0.1$ m. Note the Rayleigh diffraction distance of a disc is $ka^2/2 = 1.44$ m. A 2D spatial Fourier transform, using Equation (12), was performed over the measured surface yielding the polar distribution of the energy in the far field (see Experimental Section for complete details).

Figure 4c–f shows the normalized scattered energy distribution from both sides of the structure. The video in the supplementary material 1 shows the complete polar distribution. First, Figure 4c shows the theoretical scattering of an ideal rectangular panel, where the scattering displays a narrow angular spectrum, i.e., most of the energy is reflected/transmitted in a beam at normal direction showing a narrow beam-width, as a result of the large value of the quantity $kd \gg 1$ and the absence of surface roughness. However, when the hologram is used, as shown in Figure 4d–f using the theory, simulation and experiment, respectively, the energy is scattered in all directions covering a broad angular spectrum. This result is expected as the design field distributions present a spatial Fourier transform with uniform magnitude. There are some discrepancies, notably around ±25°, which may be caused by three factors. First, the aforementioned theoretical limitations impacting the surface phase distribution and ultimately the scattered pressure field. Second, the limitations of the experimental measurements on finite transverse plane located at some distance from the source, that results in limitations to capture the scattering at grazing angles. A detailed plot is given by Figure 4g for $\theta = 0$ rad. Lastly, neither the simulation model nor the theory takes into account for transverse waves and elasticity of the solid material beyond pressure waves. However, one important remark is that since wavefront incidence angle is normal to the structure surface, the expected mode conversion from pressure waves to shear waves is low, and the contribution of transverse modes to the total scattered energy might remain low. In this sense, the most important contribution to the scattering comes from pressure waves and, as we observe, experimental results agree with the model. The scattered pressure fields behave as intended, despite the aforementioned discrepancies and measurement noise, where both sides of the hologram scatter waves uniformly; in similar fashion than the theoretical and numerical estimations.

To quantify the uniformity of the scattered energy, we estimated the diffusion coefficients d^R and d^T, and the normalized diffusion coefficients, d_n^R and d_n^T, and the correlation scattering coefficient δ^R and δ^T, for the reflection and transmission problems. These parameters are defined in the Experimental Section. The results are listed in **Table 1**. First, the flat panel, used as a reference, results in a low diffusion coefficient, $d^R = 0.022$. This parameter is the unity when the energy of the scattered waves is uniform along all directions, and null when the scattering function is a Dirac delta function. The large kd product results in a specular reflection. However, when the hologram is used, the diffusion coefficient is increased to about $d^R \approx d^T \approx 0.7$. The experimental and simulated values agrees with the theory. Knowing than a diffusion parameter of unity is impossible to reach using periodic repetitions of the panel due to grating lobes,[52] a value around 0.7 denotes a strong scattering behavior, akin to one obtained through a Lambertian scattering surface. As the scattering of the reference panel is highly directive, the normalized values are close to the former, $d_n^R \approx d_n^T \approx 0.7$, indicating that the hologram produces a scattering pattern much uniform than an ideal flat reflector of same dimensions.

However, the diffusion coefficient does not indicate in which particular direction the scattering is more uniform. Therefore, we

© 2025 Wiley-VCH GmbH

16163028, 0, Downloaded from https://advanced.onlinelibrary.wiley.com/doi/10.1002/adfm.202423715 by Universitaet Politecnica De Val, Wiley Online Library on [06/03/2025]. See the Terms and Conditions (https://onlinelibrary.wiley.com/terms-and-conditions) on Wiley Online Library for rules of use; OA articles are governed by the applicable Creative Commons License

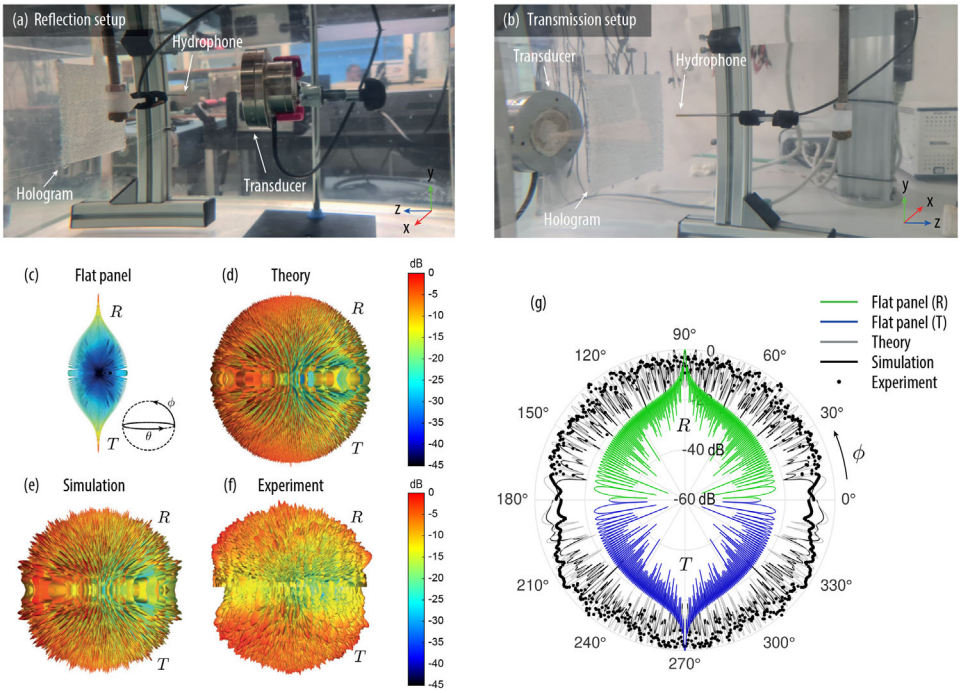


Figure 4. Experimental water tank measurement setup of the 3D-printed diffusing hologram in a) reflection and b) transmission modes. c) Scattering of a reference flat panel of same dimensions than the hologram. Scattered polar pressure distribution obtained d) theoretically, e) by simulation, and f) experimentally, respectively. g) Far-field polar pressure distribution diagram. See Video S1 (Supporting Information) for a 3D representation of the whole polar response.

calculated the correlation scattering coefficient, which indicates the dissimilarity of the scattering function of the structure and the reference scattering function of the flat reflector. We observe values close to $\delta^R \approx \delta^T \approx 0.98$, for experimental, simulated and theoretical scattering functions. If this value is close to zero, then the scattering function will be identical to the specular reflection of the reference. However, the retrieved values, close to the unity, indicates a strong reduction of the specular reflection has been produced. As can bee seen in the polar responses, they are less uniform at grazing angles. In the following, we will use the structure to reduce the specular reflection in a ultrasound imaging application.

2.5. Application for Ultrasound Imaging

Finally, the hologram was used to improve image quality in ultrafast ultrasound imaging systems. A 256-channel ultrasound acquisition platform (Vantage 256, Verasonics, Kirkland, USA) was used. A 128-channel, 2-7 MHz probe (IP-104, Sonic Concepts, USA), as shown in **Figure 5**, was connected to the Vantage. An ultrafast plane wave imaging procedure was set using a frame rate of 10 000 frames per second, and radio-frequency signals were acquired using a 28-MHz sampling frequency. By using ultrafast ultrasound sequences, the dynamic processes can be studied in a fine temporal scale, enabling techniques such as functional ultrasound, ultrasound localization microscopy, or ultrasound elastography. However, these high frame rates can result in interferences when imaging in highly reverberating environments, such as a simple water tank. Here, experiments were set, one for multiple bubble imaging and localization, and a second for soft-tissue imaging.

First, bubbles were generated in a water tank using a 30-mL Luer slip syringe. Using ultrafast plane-wave imaging, echoes were acquired at 10 000 Hz and frames were composed using delay-and-sum. The resulting images, as shown in Figure 5a,b, show intense artifacts. These interferences are mainly produced by specular reflections on the reflecting walls, and cannot be efficiently filtered by singular-value-decomposition filters. When these data is used for bubble localization and tracking, the retrieved bubble localization image is noisy and these traces are not clear or even absent, as shown in Figure 5e,f. To mitigate this, the diffusing metasurface is placed at the bottom of the tank. Then, energy is evenly reflected in all directions, greatly reducing the energy specular component. In this way, image quality is restored, and individual bubbles can be clearly imaged without interferences, as shown in Figure 5c,d. This artifact-free images can then be used for bubble localization and tracking, as shown

Table 1. Scattering coefficients of the bidirectional hologram obtained by the theory, simulation and experiments. The diffusion coefficient of the flat panel, used for normalization, is $d_r^R = d_r^T = 0.022$ (note that $d_n^R = d_n^T = 0$ and $\delta^T = \delta^R = 0$ for the rectangular reference panel).

	Reflection			Transmission		
	d^R	d_n^R	δ^R	d^T	d_n^T	δ^T
Theory	0.672	0.665	0.939	0.677	0.669	0.982
Simulation	0.744	0.738	0.998	0.767	0.761	0.999
Experiment	0.658	0.651	0.999	0.726	0.721	0.975

© 2025 Wiley-VCH GmbH

16163028, 0, Downloaded from https://advanced.onlinelibrary.wiley.com/doi/10.1002/adfm.202423715 by Universitaet Politecnica De Val, Wiley Online Library on [06/03/2025]. See the Terms and Conditions (https://onlinelibrary.wiley.com/terms-and-conditions) on Wiley Online Library for rules of use; OA articles are governed by the applicable Creative Commons License

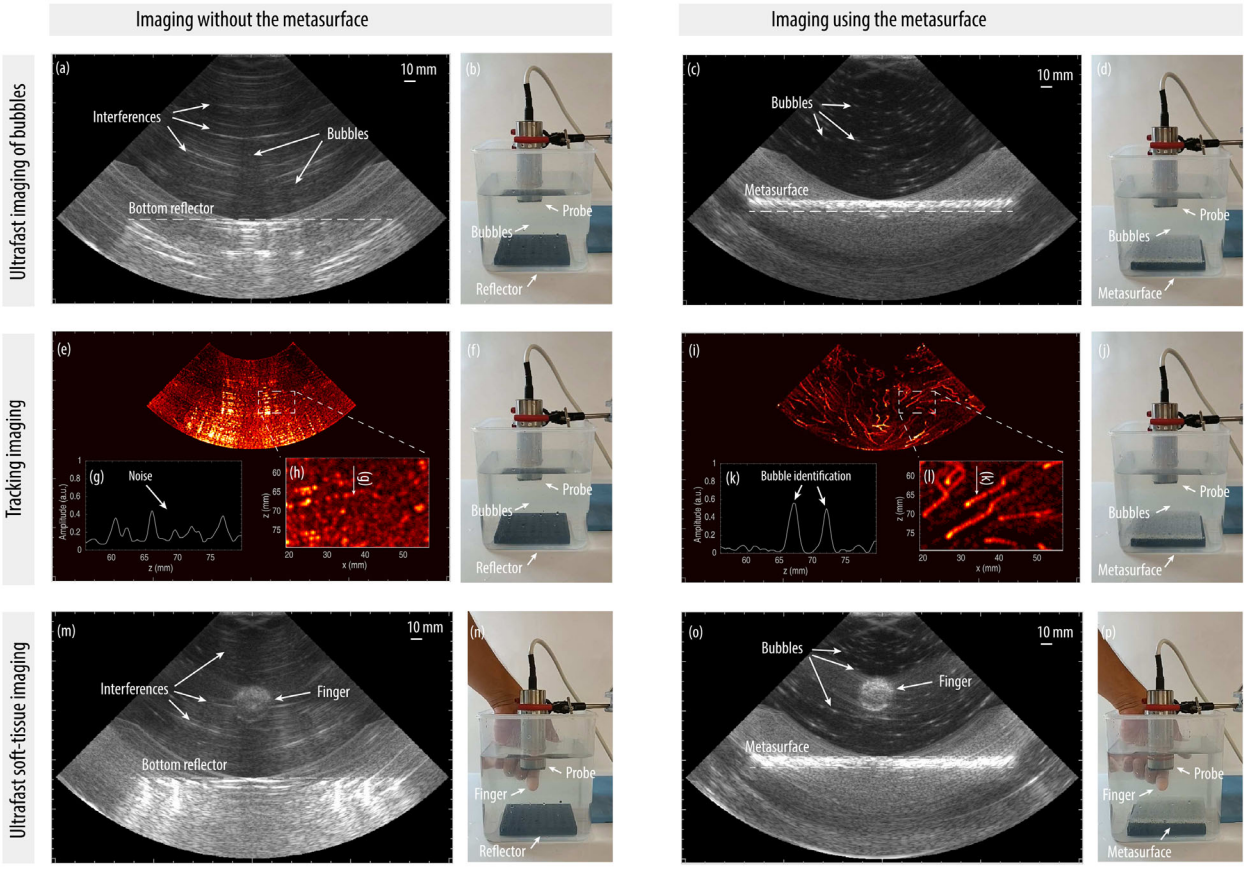


Figure 5. a) Example of an ultrasound image and b) setup obtained in a water tank in which the reflections at the bottom of the tank produces interferences on the image. c,d) Image by using the bidirectional hologram at the bottom of the tank to improve image quality (see S2 for the video, Supporting Information). e,f) Individual bubble localization and tracking, g,h) when reflections are present localization is hardly achieved. i,j) Individual bubble localization and tracking using the metasurface, k,l) using the bidirectional hologram, bubbles can be accurately localized and tracked. m,n) Example of image of a soft tissue (tip of a finger) and surrounding bubbles without using the diffuser. o,p) Same setup using the bidirectional hologram (See S3 for the video, Supporting Information).

in Figure 5i–l. Using the metasurface, bubble traces are retrieved with accuracy, enabling bubble position estimations in strong reverberating environments. Because motion is important in ultrafast imaging, a video is provided in the S2 (Supporting Information) where it is shown that bubble positions can be tracked in this reverberating environment only when using the hologram. It is worth noting here that the the scattered energy is given by $(1-\alpha)\delta^R$, and the energy of the specular reflection is given by $(1-\alpha)(1-\delta^R)$, where $\alpha = 1 - |R|^2 - |T|^2$ is the absorption coefficient.[53] Therefore, the energy reflected in the specular reflection is lower than the energy of the total scattered field, i.e., the ratio of energies is given by $(1-\delta^R)/\delta^R$. For example, the ratio of specular to total scattered energy is −30 dB for the experiment ($\delta^R = 0.999$), while it becomes −27.0 dB in the simulations and −12.1 dB in the theoretical calculations. In this way, an efficient diffuser have the potential to reduce artifacts from reverberation by reducing the energy of the specular reflections, as demonstrated by the imaging experiment.

The same procedure can be used to image in-vivo tissues in the absence (Figure 5m,n), and using the hologram (in Figure 5o,p) to produce diffuse reflections. Here, the tip of a finger is imaged. Note that the finger is a complex structure composed of soft (skin, muscles, tendons) and hard (bones) tissues. Therefore, ultrasound imaging using a standard delay-and-sum beamformer is only accurate to image the external soft-tissue layers of the finger. In this case, aberration free image can also be obtained in this environment just after introducing the hologram. In this case, some remaining bubbles can be also identified. Note that in ultrasound imaging the gray level usually indicates the energy of the echoes rather than their amplitude, and it is usually represented in a logarithmic (or highly compressed) color scale. Therefore, any small-amplitude echo, as those produced by the specular reflections, will be displayed. The absence of image artifacts indicates that the structure is indeed evenly scattering the energy. A video is provided in the S3 (Supporting Information) for the case of soft tissue imaging.

3. Discussion

This work presents a bidirectional asymmetric ultrasonic hologram that produces a uniform scattering profile over the whole angular spectrum, where this flat structure is designed simultaneously for reflected and transmitted waves. The design framework of such hologram follows a multi-objective optimization

© 2025 Wiley-VCH GmbH

16163028, 0, Downloaded from https://advanced.onlinelibrary.wiley.com/doi/10.1002/adfm.202423715 by Universitaet Politecnica De Val, Wiley Online Library on [06/03/2025]. See the Terms and Conditions (https://onlinelibrary.wiley.com/terms-and-conditions) on Wiley Online Library for rules of use; OA articles are governed by the applicable Creative Commons License

16163028, 0, Downloaded from https://advanced.onlinelibrary.wiley.com/doi/10.1002/adfm.202423715 by Universitaet Politecnica De Val, Wiley Online Library on [06/03/2025]. See the Terms and Conditions (https://onlinelibrary.wiley.com/terms-and-conditions) on Wiley Online Library for rules of use; OA articles are governed by the applicable Creative Commons License

procedure to find the geometrical parameters of the structure that produce the target reflection and transmission phase values. This method allows the pixel-wise tuning of the phase of the transmitted and reflected field at the two interfaces of the structure. In this way, the optimized building blocks can be used to replicate any desired reflection and transmission phase profiles. In the work herein, the case of an ideal holographic diffuser based on a quadratic residue sequence has been demonstrated. Theoretical, numerical and experimental results show that the scattering function is uniform. The results show a normalized diffusion coefficient around $d_n \approx 0.7$ and a correlation scattering coefficient of $\delta \approx 0.98$, indicating that the scattering function is uniform, and almost no energy is scattered in the specular direction.

An example application of this ultrasonic diffuser is provided to reduce the reverberation artifacts during ultrafast imaging in a water bath. Ultrafast ultrasound imaging has enabled groundbreaking ultrasound imaging techniques such as ultrasound localization microscopy for super-resolution imaging,[54] functional ultrasound to image brain activity in real-time,[55] or advanced elastography methods.[56] These techniques rely on the highly sensitive tracking of micro-bubbles, red blood cells, or tissue movements, respectively. However, in reverberating environments, such as a simple water tank, strong reflections can introduce artifacts, as shown in the application example. By using the acoustic hologram, energy is scattered uniformly by the diffusely reflecting surface, the acoustic intensity of the specular reflection is strongly reduced and, then, the image artifacts during ultrafast ultrasound imaging are minimized. In this way, by using this structure, the bubbles can be tracked with accuracy and tissues can be imaged without artifacts. This kind of tunable bidirectional hologram could be further optimized to create tailored scattering wave fields for one or both directions, with potential applications ranging from biomedical ultrasound therapy,[26] to low-cost ultrasonic imaging systems by using compressive sensing.[34]

4. Experimental Section

Model and Theory: We consider an ultrasonic hologram composed of a discrete spatial distribution of building blocks made of a monolithic elastic blocks (polymer) with different height embedded in a fluid (water). The scheme is shown in Figure 1.

On the one hand, we consider first a 1D problem for each constituting building block of the hologram. Unit cells are made of a monolithic polymer block of length h, surrounded by two water blocks of lengths d_1 and d_2, respectively as shown in Figure 1c. The sound pressures, p, and normal particle velocities, v_z, at $z = 0$ and at $z = L$ can be modeled by means of the Transfer Matrix Method (TMM).[57] Due to the lateral dimensions of the building blocks ($\Delta x = \Delta y = 700\mu m$), and normal incidence, we assume plane wave propagation for each element. This implies that we consider each building block is independent of each other in the structure and considered as an equivalent fluid. Such approximation can be made due to the small difference in impedance between the fluid and solid media, with a polymer-to-water impedance ratio $Z_p/Z_w \approx 1$. In addition, shear waves in the solid can also be neglected due to normal incidence. Therefore, the transfer matrix $\mathbf{T}$ of the building block can be derived, and the reflection and transmission coefficients calculated. The system can thus be written as

$$\begin{bmatrix} p \\ v_z \end{bmatrix}_{z=0} = T \begin{bmatrix} p \\ v_z \end{bmatrix}_{z=L} = \begin{bmatrix} T_{11} & T_{12} \\ T_{21} & T_{22} \end{bmatrix} \begin{bmatrix} p \\ v_z \end{bmatrix}_{z=L} \tag{7}$$

where $\mathbf{T}$ is given by the product of the transfer matrices of the different media constituting each building block in the hologram, i.e.,

$$T = T_{d_1} T_h T_{d_2} \tag{8}$$

where $\mathbf{T}_d$ and $\mathbf{T}_h$ are the transfer matrices of the fluid and solid blocks, respectively, as shown in Figure 1c. The total length $L = h + d_1 + d_2$ is constant for all the designed building blocks. Each transfer matrix block, $\mathbf{T}_i$, can be written as a homogeneous and isotropic fluid, expressed as

$$\mathbf{T}_n = \begin{bmatrix} \cos(k_n z_n) & \mathrm{i} Z_n \sin(k_n z_n) \\ \frac{\mathrm{i}}{Z_n} \sin(k_n z_n) & \cos(k_n z_n) \end{bmatrix} \tag{9}$$

where $\mathrm{i} = \sqrt{-1}$, $n = d_1, d_2, h$, $k_n = \omega/c_n$ and $Z_n = \rho_n c_n$ are the wavenumber and characteristic impedance of the medium, respectively, with ω the angular frequency, $c_n = \sqrt{K_n/\rho_n}$ the propagating sound speed, K_n the bulk modulus of the medium, and ρ_n the density, in the n-th media (water when $z_n = d_1$ or $z_n = d_2$, and polymer when $z_n = h$).

Considering the continuity of pressure and velocity at $z = 0$ and $z = L$ in a reciprocal transmission problem (meaning that the system is linear and time-invariant and the transmission does not depend on the direction of the incident wave) and accounting for the asymmetry of the hologram (meaning that there is no forced mirror symmetry with respect to $z = L/2$), the transmission and upward reflection coefficients, T and R (see Figure 1c), can be expressed in function of the transfer matrix elements outlined in Equation (7), as[57]

$$T_{\mathrm{TMM}} = \frac{2}{T_{11} + T_{12}/Z_0 + T_{21} Z_0 + T_{22}} \tag{10}$$

$$R_{\mathrm{TMM}} = \frac{T_{11} + T_{12}/Z_0 - T_{21} Z_0 - T_{22}}{T_{11} + T_{12}/Z_0 + T_{21} Z_0 + T_{22}} \tag{11}$$

It must be noted that the respective phases of the transmission and reflection coefficients are separated by a travel distance L, which implies that a reference phase origin for both phases must be chosen when writing down the fields from each side of the 1D building block. In this case a phase origin at $z = 0$ has been chosen for calibrating both coefficients.

Following Fraunhofer's diffraction theory, the far-field scattered sound pressure distribution can be obtained as a spatial Fourier transform of the pressure at the surface, e.g., the spatial Fourier transform of the reflection and transmission coefficients, respectively. In this case, the far-field pressure distribution, $p_s(\theta, \phi)$, where θ and ϕ are the azimuth and elevation angles, respectively, of a radiating rectangular surface producing a spatially dependent reflection and transmission coefficients, $\xi(x, y)$, of size $2a$ and $2b$ in the x and y directions, respectively, can be calculated using the Fraunhofer integral[58]

$$p_s(\theta, \phi) = \int_{-a}^{a} \int_{-b}^{b} \xi(x, y) e^{\mathrm{i}k(x \sin\phi \sin\theta + y \sin\phi \cos\theta)} \mathrm{d}x\mathrm{d}y \tag{12}$$

The subindex $s = R, T$ represents the reflection and transmission problems, respectively, and $\xi(x, y) = R_{\mathrm{TMM}}(x, y)$ for the reflection and $\xi(x, y) = T_{\mathrm{TMM}}(x, y)$ for the transmission problem.

Experimental Methods: For the experimental validation, a larger 3D-printed hologram, with $N = 53$ repeated $M = 3$ times (see Figure 1a), was designed for a frequency of 1.1 MHz. The hologram was built using stereolithography techniques (SLA) which used a transparent polymer previously characterized (See Supporting Information). A high N value was taken in order to produce a large structure for ultrasonic measurements, where no more than $M = 3$ repetitions were desired to reduce diffraction grating lobes due to periodicity. A larger N also helps design a hologram with a much more uniform spatial Fourier transform due to the nature of pseudo-random sequences. A custom 1.1-MHz piezoelectric transducer (PZT26, Ferroperm, Denmark) with aperture of $2a = 50$ mm, was used to

 © 2025 Wiley-VCH GmbH

generate ultrasound. The transducer was excited with a 20-cycle sinusoidal pulse burst at 1.1 MHz using a signal generator (model PXI-5412, 14-bit, 100 MS/s, National Instruments, USA) and amplified with a linear radio-frequency amplifier (model 1040L, 400 W, 55 dB, ENI, Rochester, NY, USA). Acoustic fields were measured with a polyvinylidene difluoride (PVDF) hydrophone (model HNR500, Onda, Castellon), calibrated from 500 kHz to 4 MHz, mounted on a 3D axis system (5-µm resolution, PI Micos GmbH, Germany). The hologram was immersed in a degassed and distilled water tank at controlled room temperature (22 °C). Degassed water flow was used to eliminate the remaining bubbles trapped at the hologram surface. The hydrophone was placed on either sides of the hologram depending on the reflection or transmission measurement situation, as illustrated in Figure 4a,b. Acoustic pressure was measured in front of the hologram in the x and y directions in order to map the far-field pressure plane distribution. In this way, the measurements were acquired in a transverse (x, y) square plane covering 140 mm, using a spatial step of 0.2 mm, located in the near-field at $z = 0.1$ m, note the Rayleigh diffraction distance of a disc is $ka^2/2 = 1.44$ m. On the one hand, the z distance was chosen large enough to provide a temporal lag to eliminate the direct field by temporal windowing for reflection mode, and the reflections between the hydrophone-sample. On the other, this distance was chosen small enough to capture a broad angular spectrum. A 2D spatial Fourier transform, using Equation (12), was performed over the measured surface yielding the polar distribution of the energy in the far field.

Diffusion Coefficient: The calculation of the diffusion coefficient follows the standardized procedures described in ref. [59]. The acquired waveforms were deconvolved and impulse response were obtained. Temporal windowing was applied to eliminate the direct field and the spectrum at each location was calculated using fast-Fourier transforms. Then, the scattering in the far-field $p_s(\theta, \phi)$ was calculated using Equation (12). The diffusion coefficient, d^s, is given by

$$d^s = \frac{\left(\sum_{m=1}^{M} |p_s|\right)^2 - \sum_{m=1}^{M} |p_s|^2}{(M-1)\sum_{m=1}^{M} |p_s|^2} \tag{13}$$

were $s = (R, T)$ for the reflection and transmission problems, M is the total number of measurements and m is the index of each measurement. In order to compensate the non-uniformity of the grid in spherical coordinates, the following modification[59] is used

$$d^s = \frac{\left(\sum_{m=1}^{M} A_m|p_s|\right)^2 - \sum_{m=1}^{M} A_m|p_s|^2}{\left(\sum_{m=1}^{M} A_m - 1\right)\sum_{m=1}^{M} A_m|p_s|^2} \tag{14}$$

where

$$A_m = \begin{cases} \sin\left(\frac{\Delta\phi}{2}\right), & \text{for } \theta_m = 0, \\ 2\sin(\theta_m)\sin\left(\frac{\Delta\theta}{2}\right), & \text{for } 0 < \theta_m < \pi/2, \\ \frac{4\pi}{\Delta\phi}\sin\left(\frac{\Delta\theta}{4}\right)^2, & \text{for } \theta_m = \pi/2 \end{cases} \tag{15}$$

The scattered field was estimated for both the hologram and a rectangular reference panel of same dimensions. For the reflection problem, a rigid rectangular reflector is used. For the transmission, a rectangular aperture is used as the reference. Then, and the corresponding diffusion coefficients were calculated. Finally, the normalized diffusion coefficient, d_n, was obtained as

$$d_n^s = \frac{d_s - d_r}{1 - d_r(\omega)} \tag{16}$$

where d_s and d_r are the diffusion coefficient of the hologram and the rectangular reflector, respectively. This coefficient measures the uniformity of the scattering.

Correlation-Scattering Coefficient: Finally, the correlation-scattering coefficient δ was calculated using the measured scattering as.[53]

$$\delta^s = 1 - \frac{\left|\sum_{m=1}^{M} p_s p_r^*\right|^2}{\sum_{m=1}^{M} |p_s|^2 \sum_{m=1}^{M} |p_r|^2} \tag{17}$$

where p_s and p_r are scattering of the hologram and the reference reflector for the m-th grid point, respectively, and (*) is the complex conjugate. This coefficient measures the correlation between the scattering of the structure and that of a flat panel of same dimensions.

Quadratic Phase Modulation and Even Spacing of Diffraction Lobes: The phase distribution that corresponds to the quadratic residue sequence is given by

$$\phi_n = \frac{2\pi r_n}{p} \tag{18}$$

where r_n represents the n-th quadratic residue in the sequence and ϕ_n is the phase shift applied at the n-th position. The set of phase shifts corresponds to the quadratic residues modulo p mapped to phase values. This set is periodic with period p, meaning that after p elements, the sequence repeats. The diffraction pattern produced by this phase modulation can be understood through the diffraction angle θ, which is related to the phase shift by the grating equation for diffraction:

$$d\sin(\theta) = m\lambda \tag{19}$$

where d is the spacing between the phase-modulating elements (e.g., a metasurface), λ is the wavelength, and m is the diffraction order. When the phase shifts follow the quadratic residue sequence, the resulting diffraction lobes are evenly spaced because the phase shifts themselves are distributed in a regular, cyclic manner due to the periodicity of the quadratic residue sequence. To quantify the angular spacing of the lobes, we consider the angular separation $\Delta\theta$ between two successive diffraction orders. Because the phase shifts are distributed according to the quadratic residues, the resulting angular separation is constant, leading to evenly spaced diffraction lobes. Specifically, if the phase sequence is applied to a surface with periodicity d, the resulting diffraction angles are separated by a constant value $\Delta\theta$, given by

$$\Delta\theta = \frac{\lambda}{d} \tag{20}$$

Thus, the cyclic nature of quadratic residues not only governs the spacing between the diffraction lobes but also ensures a balanced energy distribution, making them ideal for applications where uniform scattering is desired.

Supporting Information

Supporting Information is available from the Wiley Online Library or from the author.

Acknowledgements

E.-B. and J.-P. G. contributed equally to this work. The collaboration between the authors of this article was made possible thanks to Institut d'Acoustique – Graduate School (IAGS) project (ANR-17-EURE-0014) from the Laboratoire d'Acoustique du l'Université du Mans (LAUM) for

© 2025 Wiley-VCH GmbH

16163028, 0, Downloaded from https://advanced.onlinelibrary.wiley.com/doi/10.1002/adfm.202423715 by Universitaet Politecnica De Val, Wiley Online Library on [06/03/2025]. See the Terms and Conditions (https://onlinelibrary.wiley.com/terms-and-conditions) on Wiley Online Library for rules of use; OA articles are governed by the applicable Creative Commons License

the support and mobility. The authors gratefully acknowledge the ANR-RGC METARoom (ANR-18-CE08-0021) project and N.J and V.R-G acknowledges financial support from Conselleria de Innovación, Universidades, Ciencia y Sociedad Digital de la Generalitat Valenciana through project CIAICO/2022/052 of the Programa para la promoción de la investigación científica, el desarrollo tecnológico y la innovación en la Comunitat Valenciana. This research has been supported by the Ministerio Español de Ciencia e Innovación grant RYC2021-034920-I and Agencia Estatal de Investigación grants PID2022-142719OB-C21 and CNS2023-145707 funded by MCIN/AEI/10.13039/501100011033 and grant PID2023-146237NB-I00 funded by MICIU/AEI/ 10.13039/501100011033. Funding for open access charge: CRUE-Universitat Politècnica de València.

Conflict of Interest

The authors declare no conflict of interest.

Author Contributions

E.B., J-P.G., V.R-G., and N.J. conceived the project, under the direction of N.J. E.B, V.R.-G and N.J wrote the code for the theoretical and numerical data. E.B performed the multi-objective optimization and provided the dimensions of the ultrasonic lens. J.R-S 3D-printed the sample and performed the experimental measurements along with N.J, as well as provided details on the experimental apparatus. N.J analyzed the experimental data. E.B, and N.J. wrote the initial manuscript with input from all authors. E.B, V.R.-G and N.J. prepared the revised version and the response to the referees with input from all authors. All authors have reviewed and commented on the final manuscript.

Data Availability Statement

The data that support the findings of this study are available from the corresponding author upon reasonable request.

Competing Interests

There are no competing interests to declare.

Data and Materials Availability

Data presented in this work is available upon reasonable request addressed to E.B. and N.J.

Keywords

acoustic diffusers, holograms, metamaterials, ultrasonic imaging

Received: December 3, 2024
Revised: January 31, 2025
Published online:

[1] K. Melde, A. Mark, T. Qiu, P. Fischer, *Nature* **2016**, *537*, 518.
[2] M. Brown, D. Nikitichev, B. Treeby, B. Cox, *Appl. Phys. Lett.* **2017**, *110*.
[3] M. D. Brown, B. T. Cox, B. E. Treeby, *Appl. Phys. Lett.* **2020**, *116*, 261901.
[4] T. Fushimi, K. Yamamoto, Y. Ochiai, *Sci. Rep.* **2021**, *06*, 11.
[5] H. Y. Zou, Y. Ge, K. Q. Zhao, Y. J. Lu, Q. r. Si, S. Q. Yuan, et al., *Adv. Mater.* **2024**, 2401738.
[6] A. Sallam, V. C. Meesala, M. R. Hajj, S. Shahab, *Appl. Phys. Lett.* **2021**, *119*.
[7] X. Ren, Q. Zhou, J. Huang, Z. Xu, X. Liu, *Ultrasonics* **2023**, *134*, 107074.
[8] Y. Li, B. Liang, Z. Gu, X. Y. Zou, J. C. Cheng, *Sci. Rep.* **2013**, *3*, 2546.
[9] G. Memoli, M. Caleap, M. Asakawa, D. Sahoo, B. Drinkwater, S. Subramanian, *Nat. Commun.* **2017**, *8*, 14608.
[10] M. D. Brown, *Appl. Phys. Lett.* **2019**, *115*.
[11] M. D. Brown, B. T. Cox, *Phys. Rev. Appl.* **2023**, *19*, 044032.
[12] M. D. Brown, B. T. Cox, B. E. Treeby, *Appl. Phys. Lett.* **2017**, *111*, 244101.
[13] J. Zhang, Y. Tian, Y. Cheng, X. Liu, *Appl. Phys. Lett.* **2020**, *116*.
[14] A. Marzo, B. W. Drinkwater, *Proc. Natl. Acad. Sci. USA* **2019**, *116*, 84.
[15] Z. Ma, A. W. Holle, K. Melde, T. Qiu, K. Poeppel, V. M. Kadiri, et al., *Adv. Mater.* **2020**, *32*, 1904181.
[16] Y. Gu, C. Chen, J. Rufo, C. Shen, Z. Wang, P. H. Huang, et al., *ACS nano* **2020**, *14*, 14635.
[17] M. A. Ghanem, A. D. Maxwell, D. Dalecki, O. A. Sapozhnikov, M. R. Bailey, *Sci. Rep.* **2023**, *13*, 9160.
[18] K. Melde, E. Choi, Z. Wu, S. Palagi, T. Qiu, P. Fischer, *Adv. Mater.* **2018**, *30*, 1704507.
[19] K. Melde, H. Kremer, M. Shi, S. Seneca, C. Frey, I. Platzman, et al., *Sci. Adv.* **2023**, *9*, eadf6182.
[20] S. Jiménez-Gambín, N. Jiménez, J. M. Benlloch, F. Camarena, *Sci. Rep.* **2019**, *9*, 20104.
[21] Q. Zhou, J. Zhang, X. Ren, Z. Xu, X. Liu, *Appl. Phys. Lett.* **2020**, *116*.
[22] S. Gao, Y. Li, C. Ma, Y. Cheng, X. Liu, *Nat. Commun.* **2021**, *12*, 2006.
[23] G. Reardon, B. Dandu, Y. Shao, Y. Visell, *Sci. Adv.* **2023**, *9*, eadf2037.
[24] R. Hirayama, G. Christopoulos, D. Martinez Plasencia, S. Subramanian, *Sci. Adv.* **2022**, *8*, eabn7614.
[25] L. Cox, K. Melde, A. Croxford, P. Fischer, B. W. Drinkwater, *Phys. Rev. Appl.* **2019**, *12*, 064055.
[26] S. Jiménez-Gambín, N. Jiménez, J. M. Benlloch, F. Camarena, *Phys. Rev. Appl.* **2019**, *12*, 014016.
[27] D. Andrés, J. Vappou, N. Jiménez, F. Camarena, *Appl. Phys. Lett.* **2022**, *120*, 084102.
[28] D. Andrés, I. Rivens, P. Mouratidis, N. Jiménez, F. Camarena, G. Ter Haar, *Cancers* **2023**, *15*, 2540.
[29] C. Cengiz, S. Shahab, *J. Phys. D: Appl. Phys.* **2024**, *57*, 365501.
[30] J. Kim, S. Kasoji, P. G. Durham, P. A. Dayton, *Appl. Phys. Lett.* **2021**, *118*.
[31] S. Jiménez-Gambín, N. Jiménez, A. N. Pouliopoulos, J. M. Benlloch, E. E. Konofagou, F. Camarena, *IEEE Trans. Biomed. Eng.* **2021**, *69*, 1359.
[32] Z. Hu, Y. Yang, L. Yang, Y. Gong, C. Chukwu, D. Ye, et al., *Proc. Natl. Acad. Sci. USA* **2024**, *121*, e2402200121.
[33] S. Jiménez-Gambín, N. Jiménez, F. Camarena, *Phys. Rev. Appl.* **2020**, *14*, 054070.
[34] P. Kruizinga, P. Meulen, A. Fedjajevs, F. Mastik, G. Springeling, N. Jong, et al., *Sci. Adv.* **2017**, *12*, e1701423.
[35] N. Lamothe, D. Andrés, A. Carrión, F. Camarena, J. A. Pineda-Pardo, N. Jiménez, *Appl. Acoust.* **2024**, *224*, 110144.
[36] M. D. Brown, B. S. Generowicz, S. Dijkhuizen, S. K. Koekkoek, C. Strydis, J. G. Bosch, et al., *Sci. Adv.* **2024**, *10*, eadk7957.
[37] N. Jiménez, J. P. Groby, V. Romero-García, *Sci. Rep.* **2021**, *11*, 10217.
[38] M. R. Schroeder, *J. Acoust. Soc. Am.* **1975**, *57*, 149.
[39] T. Cox, P. D'Antonio, *Build. Acoust.* **2003**, *10*, 1.
[40] N. Jiménez, T. J. Cox, V. Romero-García, J. P. Groby, *Sci. Rep.* **2017**, *7*, 5389.
[41] L. Claes, H. Zeipert, P. Koppa, T. Tröster, B. Henning, *Proc. Meet. Acoust.* **2017**, *32*, 030004.

 © 2025 Wiley-VCH GmbH

16163028, 0, Downloaded from https://advanced.onlinelibrary.wiley.com/doi/10.1002/adfm.202423715 by Universitaet Politecnica De Val, Wiley Online Library on [06/03/2025]. See the Terms and Conditions (https://onlinelibrary.wiley.com/terms-and-conditions) on Wiley Online Library for rules of use; OA articles are governed by the applicable Creative Commons License

[42] A. Vasan, F. Allein, M. Duque, U. Magaram, N. Boechler, S. H. Chalasani, et al., *Advanced NanoBiomed Research* **2022**, *2*, 2100135.
[43] Y. Tang, Y. Zhang, B. Xie, H. Cheng, J. Tian, S. Chen, *Phys. Rev. Appl.* **2022**, *17*, 044027.
[44] F. Ju, X. Zou, S. Xue, S. Y. Qian, *Appl. Phys. Express* **2023**, *16*, 074003.
[45] H. Cheng, J. Guo, *Appl. Phys. Lett.* **2024**, *124*.
[46] J. Huang, P. Dupont, A. Undurti, J. Triedman, R. Cleveland, *Ultrasound Med. Biol.* **2006**, *32*, 721.
[47] D. Arslan, A. Rahimzadegan, S. Fasold, M. Falkner, W. Zhou, M. Kroychuk, et al., *Adv. Mater.* **2022**, *34*, 2105868.
[48] T. J. Cox, P. D'Antonio, in: Acoustic Absorbers and Diffusers: Theory, Design and Application Crc Press, **2009**, pp. 295–306.
[49] B. E. Treeby, B. T. Cox, *J. Acoust. Soc. Am.* **2010**, *127*, 2741.
[50] D. Andrés, A. Carrión, F. Camarena, N. Jiménez, *Phys. Rev. Appl.* **2023**, *20*, 044071.
[51] O. A. Sapozhnikov, S. A. Tsysar, V. A. Khokhlova, W. Kreider, *J. Acoust. Soc. Am.* **2015**, *138*, 1515.
[52] E. Ballestero, N. Jiménez, J. P. Groby, H. Aygun, S. Dance, V. Romero-García, *Appl. Phys. Lett.* **2021**, *119*, 044101.
[53] T. J. Cox, P. D'Antonio, Acoustic absorbers and diffusers: theory, design and application. 3rd ed. CRC Press, **2016**.
[54] C. Errico, J. Pierre, S. Pezet, Y. Desailly, Z. Lenkei, O. Couture, M. Tanter, *Nature* **2015**, *527*.
[55] E. Macé, G. Montaldo, I. Cohen, M. Baulac, M. Fink, M. Tanter, *Nat. Methods* **2011**, *8*, 662.
[56] M. Tanter, M. Fink, *IEEE transactions u. ltrasonics. on, ferroelectrics, and frequency control* **2014**, *61*, 102.
[57] N. Jiménez, J. P. Groby, V. Romero-García, in: *Acoustic Waves in Periodic Structures, Metamaterials, and Porous Media: From Fundamentals to Industrial Applications Cham*, (Eds.: N. Jiménez, O. Umnova, J. P. Groby) Springer, Switzerland **2021**, pp. 103–164.
[58] T. D. Rossing, F. Dunn, W. M. Hartmann, D. M. Campbell, N. H. Fletcher, *Springer Handbook of Acoustics*, 1st edn. Springer C. ompany. Publishing, Incorporated **2007**.
[59] ISO 17497–2:2012. Acoustics – Sound-scattering properties of surfaces – Part 2: Measurement of the directional diffusion coefficient in a free field. Geneva, Switzerland: International Organization for Standardization, **2012**.

© 2025 Wiley-VCH GmbH

16163028, 0, Downloaded from https://advanced.onlinelibrary.wiley.com/doi/10.1002/adfm.202423715 by Universitaet Politecnica De Val, Wiley Online Library on [06/03/2025]. See the Terms and Conditions (https://onlinelibrary.wiley.com/terms-and-conditions) on Wiley Online Library for rules of use; OA articles are governed by the applicable Creative Commons License